Tracing snowlines and C/O ratio in a planet-hosting disk: ALMA molecular line observations towards the HD 169142 disk

Booth, A.S.; Law, C.J.; Temmink, M.; Leemker, M.; Macías, E.

A&A, 678, A146 (2023)
https://doi.org/10.1051/0004-6361/202346974

Astronomy & Astrophysics

Tracing snowlines and C/O ratio in a planet-hosting disk

ALMA molecular line observations towards the HD 169142 disk

Alice S. Booth[1], Charles J. Law[2], Milou Temmink[1], Margot Leemker[1], and Enrique Macías[3]

[1] Leiden Observatory, Leiden University, 2300 RA Leiden, The Netherlands
e-mail: abooth@strw.leidenuniv.nl; alice.booth@cfa.harvard.edu
[2] Center for Astrophysics – Harvard & Smithsonian, 60 Garden St., Cambridge, MA 02138, USA
[3] European Southern Observatory, Karl-Schwarzschild-Strasse 2, 85748 Garching bei München, Germany

Received 23 May 2023 / Accepted 13 August 2023

ABSTRACT

The composition of a forming planet is set by the material it accretes from its parent protoplanetary disk. Therefore, it is crucial to map the chemical make-up of the gas in disks to understand the chemical environment of planet formation. This paper presents molecular line observations taken with the Atacama Large Millimeter/submillimeter Array of the planet-hosting disk around the young star HD 169142. We detect N_2H^+, CH_3OH, [CI], DCN, CS, $C^{34}S$, ^{13}CS, H_2CS, H_2CO, HC_3N, and c−C_3H_2 in this system for the first time. Combining these data with the recent detection of SO and previously published DCO^+ data, we estimated the location of H_2O and CO snowlines and investigate radial variations in the gas phase C/O ratio. We find that the HD 169142 disk has a relatively low N_2H^+ flux compared to the disks around Herbig stars HD 163296 and MWC 480, indicating less CO freeze-out, and place the CO snowline beyond the millimetre disk at ≈150 au. The detection of CH_3OH from the inner disk is consistent with the H_2O snowline being located at the edge of the central dust cavity at ≈20 au. The radially varying CS/SO ratio across the proposed H_2O snowline location is consistent with this interpretation. Additionally, the detection of CH_3OH in such a warm disk adds to the growing evidence supporting the inheritance of complex ices in disks from the earlier colder stages of star formation. Finally, we propose that the giant HD 169142 b located at 37 au is forming between the CO_2 and H_2O snowlines where the local elemental make-up of the gas is expected to have C/O ≈ 1.0.

Key words. astrochemistry – protoplanetary disks – submillimeter: planetary systems – planets and satellites: composition

1. Introduction

The elemental make-up of an exoplanet's atmosphere is set by the material it accretes locally from its parent protoplanetary disk (Öberg & Bergin 2021). With ground-based high-resolution spectroscopy and the *James Webb* Space Telescope (JWST), we can infer the C/H, O/H, and C/O ratios in the atmospheres of giant exoplanets (e.g. GRAVITY Collaboration 2020; Wang et al. 2020; Reggiani et al. 2022; Bean et al. 2023). These observations now provide a direct link to unravelling the formation history of planets (see e.g. Eistrup 2023, for a review). This is particularly important as many of the gas-giant planets detected may not have formed at their current locations and have undergone migration (Dawson & Johnson 2018). A key piece of this puzzle is to measure the elemental make-up of disks, and in particular locating snowlines (CO and H_2O) at the time of planet formation.

The local gas and ice composition in a protoplanetary disk is regulated by various physical and chemical processes. The elemental make-up of the disk gas and ice varies as a function of radius and height due to the freeze-out of different molecules (Öberg et al. 2011). The growth, settling, and inward drift of dust transports volatile elements leading to an elevated gas-phase C/O > 1 in the outer regions of disks and enhanced gas-phase abundances of CO and H_2O within their respective snowlines (Du et al. 2015; Krijt et al. 2018; Zhang et al. 2019; Booth & Ilee 2019; Banzatti et al. 2020). Directly measuring the locations of snowlines is non-trivial. The most abundant and easily observable isotopologues of CO tend to be optically thick and trace gas in a layer above the disk midplane. The H_2O emission lines accessible at sub-millimetre wavelengths are weak and difficult to detect in Class II disks (Notsu et al. 2019; Bosman & Bergin 2021).

Luckily we can use other molecules as chemical tracers of the CO and H_2O snowlines. The cations DCO^+ and N_2H^+ have been used as tracers of the CO snowline, and of the two species N_2H^+ is the more robust tracer (Qi et al. 2013, 2015). N_2H^+ is destroyed by gas-phase CO, and is thus abundant in the outer disk regions where CO is frozen out (van 't Hoff et al. 2017). Due to a similar chemical relationship, HCO^+ is a chemical tracer of the H_2O snowline (e.g. Jørgensen et al. 2013; Leemker et al. 2021). Additionally, the presence of methanol (CH_3OH) indicates warm enough temperatures for the sublimation of H_2O (Booth et al. 2021b; van der Marel et al. 2021). To complement these chemical tracers, the variations in C/O across disks due to snowlines can be traced by observing pairs of molecules (e.g. SO and CS or NO and CN; Le Gal et al. 2019a, 2021; Booth et al. 2021a; Leemker et al. 2023) or by detecting molecules that have enhanced formation in elevated C/O environments (e.g. C_2H and c−C_3H_2) (Miotello et al. 2019; Guzmán et al. 2021; Bosman et al. 2021; Calahan et al. 2023).

HD 169142 is a nearby (114.0 pc) F1 star hosting an almost face-on (inclination 13°, position angle 5°) protoplanetary disk (Raman et al. 2006; Fedele et al. 2017; Gaia Collaboration 2018; Vioque et al. 2018). Multi-wavelength dust observations have revealed multiple dust rings in this transition disk that are likely

carved by forming giant planets (Fedele et al. 2017; Pohl et al. 2017; Macías et al. 2017, 2019; Pérez et al. 2019). CO gas detected within the central dust cavity points to the presence of a giant planet or low-mass companion within 10 au (Carmona 2018; Leemker et al. 2022; Garg et al. 2022; Poblete et al. 2022). In the outer disk, in a dust and gas gap, there is evidence supporting a giant planet located at 37 au (Gratton et al. 2019; Garg et al. 2022; Hammond et al. 2023). Studies of the kinematics of the CO gas in the outer disk show strong deviations from Keplerian motion in the vicinity of the planet (Garg et al. 2022), and Law et al. (2023) have recently shown evidence for shocks associated with this planet traced in SiS and SO. In this paper, we present Atacama Large Millimeter/submillimeter Array (ALMA) observations of the HD 169142 disk where we detect 13 different species. Using these data, we infer the elemental make-up of the gas and location of both the CO and H_2O snowlines in relation to these forming planets.

2. Observations

We compiled ALMA observations towards the HD 169142 disk over Bands 6, 7, and 8. Full details, including the observation dates, number of executions, baselines, integration times, and maximum recoverable scales are listed in Table A.1. All datasets were first calibrated by the ALMA staff and the subsequent data reduction, the representative angular resolution, and the molecules detected in each dataset are summarised below.

Project 2012.1.00799.S. (PI: Honda, M.) are Band 7 observations at ≈0.2″, and in these data we detect CH_3OH $J = 11_{(1,10)}-11_{(0,11)}$ and SO $J = 8_8-7_7$; SO was first presented in Law et al. (2023) along with the CO isotopologues (^{12}CO and ^{13}CO $J = 3-2$). The continuum data from this programme were initially presented in Macías et al. (2019) (for further details about the data reduction, see Law et al. 2023).

Project 2015.1.00806.S. (PI: Pineda, J.) are Band 7 observations at ≈0.03″, and in these data we detect CS $J = 6-5$. These observations also provide long baselines of the CO isotopologues (^{12}CO and ^{13}CO $J = 3-2$) (for further details on the data reduction, see Law et al. 2023).

Project 2016.1.00344.S. (PI: Perez, S.) are Band 6 observations at ≈0.2″. This project also has higher angular resolution data (≈0.02″) associated with it (see Pérez et al. 2019, for the continuum observations), but as we are searching for weak lines emission we only make use of the shorter baseline data, which are optimal for our science goals. These observations consist of five spectral windows, of which three are dedicated to the CO lines (^{12}CO, ^{13}CO, C^{18}O $J = 2-1$) and two are continuum windows centred at 218.004 GHz and 232.004 GHz. We obtained the calibrated measurement sets from the ALMA archive and performed one round of phase-only self-calibration (interval of 60 seconds) on the data after flagging the line containing channels. This resulted in only a 20% improvement in the continuum signal-to-nose ratio. In these data we detect lines of H_2CO $J = 3_{(0,3)}-2_{(0,2)}$ and $J = 3_{(2,2)}-3_{(2,1)}$, DCN $J = 3-2$, HC_3N $J = 24-23$, and c$-C_3H_2$ $J = 6_{(0,6)}-5_{(1,5)}$ and $J = 6_{(1,6)}-5_{(0,5)}$ in the 218.004 GHz continuum spectral window (see Fig. C.1).

Project 2016.1.00346.S. (PI: Tsukagoshi, T.) are Band 8 observations at ≈1.0″ and we detect CS $J = 10-9$ and [CI] $^3P_1 - ^3P_0$. The dataset contains four spectral windows that are centred at 478.651 GHz, 480.568 GHz, 489.785 GHz, and 492.195 GHz; the latter two are line spectral windows at ∼0.15 km s^{-1} spectral resolution. We obtained the calibrated measurement set from the ALMA archive and then performed self-calibration on the data. This consisted of three rounds of phase-only calibration using solution lengths (60, 20, and 6 seconds). The self-calibration yielded a signal-to-noise ratio improvement of 40% for the continuum.

Project 2018.1.01237. (PI: Macías, E.) are Band 7 observations at ≈0.8" resolution. These data target and detect DCO^+ $J = 4-3$ and N_2H^+ $J = 3-2$ and also detect DCN $J = 4-3$, ^{13}CS $J = 6-5$, C^{34}S $J = 6-5$, H_2CS $J = 8_{(1,7)}-7_{(1,6)}$, H_2CO $J = 4_{(0,4)}-3_{(0,3)}$, and the CH_3OH $J = 9_{(-1,9)}-8_{(0,8)}$ and $J = 6-5$ blend of lines. Four spectral windows were used, centred at 279.515 GHz (resolution of ∼0.15 km s^{-1}), 277.990 GHz (∼1.2 km s^{-1}), 288.147 GHz (∼0.29 km s^{-1}), and 289.990 GHz (∼17 km s^{-1}). The data were then phase-only self-calibrated using the continuum emission. For this the line emission channels were first flagged to create a continuum-only dataset. Three rounds of phase-only self-calibration were applied, with solution intervals going from *inf* (i.e. the scan duration) to 30 s. Overall, the S/N of the continuum improved from ∼900 to ∼1600. The solutions were then applied to the unflagged data. A weak detection of N_2H^+ in the images was confirmed via matched filtering and via spectral stacking with *GoFish* (see Fig. B.1; Loomis et al. 2018b; Teague 2019). The DCN, C^{34}S, and H_2CO lines and one of the CH_3OH lines are observed in a continuum spectral window at ≈17 km s^{-1} spectral resolution (see Fig. C.1).

The continuum was subtracted using *uvcontsub* with a fit order of 1 after excluding the line containing channels. The line containing channels of the continuum spectral windows were identified in an iterative process. First, we subtracted the continuum assuming that no lines were present. We then made a dirty image of the line, extracted spectra, identified any lines, and then made a new continuum subtracted measurement set flagging these channels. We performed all of the imaging in CASA version 6.2 (McMullin et al. 2007) and used Keplerian masks for the tCLEAN mask (generated with the code from Teague 2020) for lines at a spectral resolution <2 km s^{-1} and hand-drawn elliptical tCLEAN masks for other lines that were observed at a coarser spectral resolution as total line width is only a few km s^{-1} across the disk. Table 1 lists all of the properties of the molecular lines detected and the resulting images. All lines in the 2016.1.00344.S data aside from HC_3N were tapered to a 0.4″ beam to the increase S/N.

3. Results

All integrated intensity maps were generated with the same Keplerian or elliptical masks used in the imaging with no flux clipping to ensure accurate fluxes. Figure 1 presents the resulting maps for the different species detected in the HD 169142 disk. Where multiple transitions are detected we show the best image, and all of the detected transitions are shown in Fig. D.1. For comparison, we also include the 0.9 mm continuum image and ^{12}CO map from Law et al. (2023). All of the newly reported molecules show varying ring-like morphologies with the SO and CH_3OH being the most compact. Figure 2 shows the azimuthally averaged radial profiles for the same lines presented in Fig. 1. These profiles highlight a clear anti-correlation between SO and CS.

Table 1 lists the disk-integrated fluxes for all of the detected lines. We take the errors on these fluxes to be ±10% due to the uncertainty on the absolute flux calibration of ALMA. We estimate disk-averaged column densities (listed in Table 2) for all

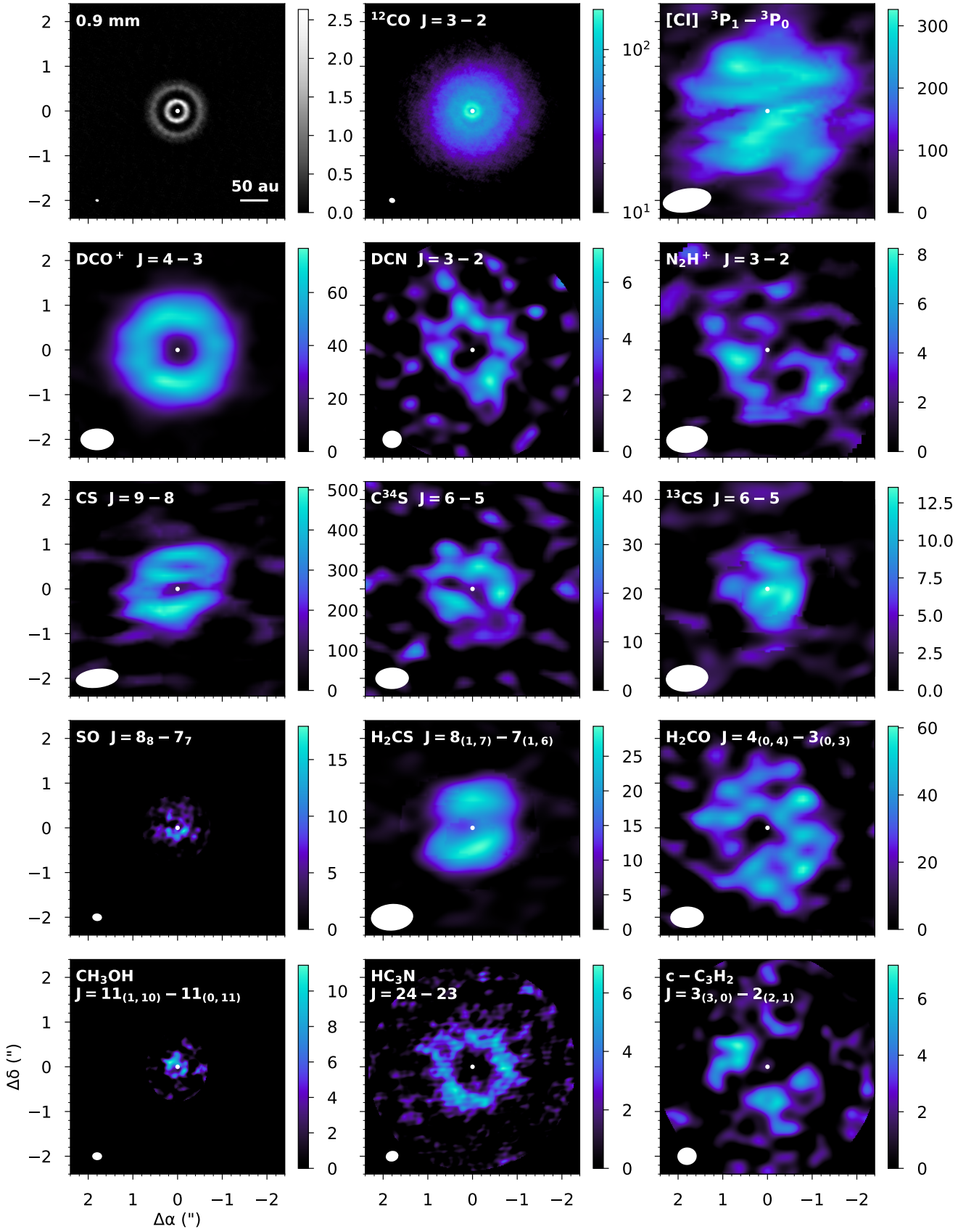

Fig. 1. Integrated intensity maps of the millimetre dust and molecular line emission from the HD 169142 protoplanetary disk. Units of the colour bars are mJy beam^{-1} for the continuum image and mJy beam^{-1} km s^{-1} for the line images aside from ^{12}CO, which is Jy beam^{-1} km s^{-1}. The beam of each observation is shown in the bottom left corner of the plots; the central dot denotes the position of the star.

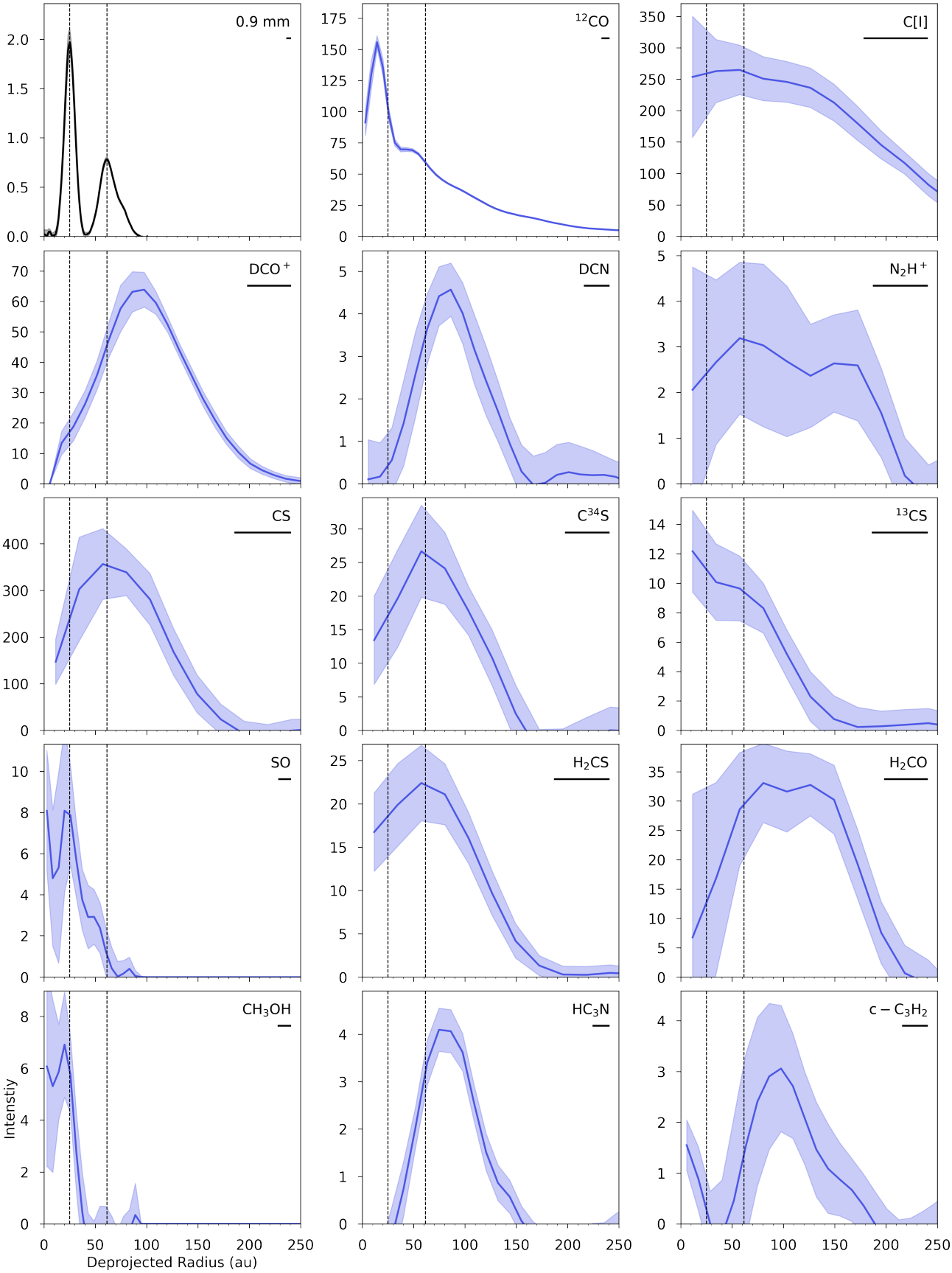

Fig. 2. Azimuthally averaged radial intensity profiles for the 0.9mm continuum emission and molecular lines from the HD 169142 disk. The specific transitions are the same as in Fig. 1. Vertical lines indicate the peak locations of the two bright continuum rings. The bar in the top right corner of the images is the 0.5× the major axis of the beam as listed in Table 1. Units of the y-axis are mJy beam^{-1} for the continuum, Jy beam^{-1} km s^{-1} for the ^{12}CO, and mJy beam^{-1} km s^{-1} for the rest of the lines.

Table 1. Molecular transitions and image properties for the detected lines in the HD 169142 disk.

Species	Transition	Frequency (GHz)	E_{up} (K)	E_{Aul} (s^{-1})	g_u	robust	Beam	δv (km s^{-1})	rms (mJy $beam^{-1}$)	Int. flux (mJy km s^{-1})
[CI]	$^3P_1$–$^3P_0$	492.160651	24	7.994×10^{-4}	3	2.0	1.07″ × 0.51″ (81°)	0.15	71.9	(7.4±0.7) × 10^3
DCO^+	J = 4–3	288.143858	35	5.858×10^{-3}	9	0.5	0.72″ × 0.46″ (89°)	0.26	2.64	970±100
DCN	J = 3–2	217.238539	21	4.575×10^{-4}	21	2.0, taper	0.41″ × 0.37″ (86°)	2.7	0.67	93.0.0±10
DCN	J = 4–3	289.644917	35	1.124×10^{-3}	27	0.5	0.73″ × 0.46″ (89°)	16.2	0.24	240.0±20
N_2H^+	J = 3–2	279.511701	27	1.259×10^{-3}	63	2.0	0.91″ × 0.58″ (85°)	0.14	2.95	55.0±6
CS(†)	J = 7–6	342.882850	66	8.368×10^{-4}	15	0.5	0.29″ × 0.26″(37°)	0.85	11.7	$\gtrsim$7 × 10^3
CS	J = 10–9	489.750921	129	2.489×10^{-3}	21	0.5	0.94″ × 0.40″ (83°)	0.15	130.7	(4.3±0.4) × 10^3
$C^{34}S$	J = 6–5	289.209066	38	4.812×10^{-4}	13	0.5	0.73″ × 0.46″ (89°)	16.2	0.23	261.0±30
^{13}CS	J = 6–5	277.455405	47	4.399×10^{-4}	26	0.5	0.73″ × 0.46″ (89°)	1.10	1.1	51±5
SO	$J = 8_8$–7_7	344.310612	88	5.186×10^{-4}	17	2.0	0.19″ × 0.14″ (84)	0.46	1.50	120±10
H_2CS	$J = 8_{(1,7)}$–$7_{1,6}$	278.887661	73	3.181×10^{-4}	51	0.5	0.73″ × 0.46″ (89°)	1.10	1.07	140±10
H_2CO	$J = 3_{0,3}$–$2_{0,2}$	218.222192	21	2.818×10^{-4}	7	2.0, taper	0.41″ × 0.37″ (86°)	2.7	0.52	480±50
H_2CO	$J = 3_{2,2}$–$3_{2,1}$	218.475632	68	1.571×10^{-4}	7	2.0, taper	0.41″ × 0.37″ (86°)	2.7	0.51	55±6
H_2CO	$J = 4_{0,4}$–$3_{0,3}$	290.623405	35	6.902×10^{-4}	9	0.5	0.73″ × 0.46″ (89°)	16.2	0.26	900±90
CH_3OH	$J = 4_{2,2}$–$3_{1,2}$	218.440050	45	4.687×10^{-5}	36	2.0	0.20″ × 0.15″ (88)	0.46	1.44	65±7
CH_3OH	$J = 9_{(-1,9)}$–$8_{(0,8)}$	278.304510	110	7.685×10^{-5}	76	0.5	0.73″ × 0.46″ (89°)	1.10	1.05	13±1
CH_3OH	blend*	290.209700	112	7.994×10^{-5}	52	0.5	0.73″ × 0.46″ (89°)	16.2	0.24	104±10
CH_3OH	$J = 11_{(1,10)}$–$11_{(0,11)}$	331.502370	169	3.929×10^{-4}	92	2.0	0.20″ × 0.15″ (88)	0.46	1.44	44±10
HC_3N	J = 24–23	218.324723	131	8.261×10^{-4}	49	2.0	0.26″ × 0.21″ (74°)	2.7	0.45	171±20
c–C_3H_2	$J = 6_{(0,6)}$–$5_{(1,5)}$	217.822148	39	5.934×10^{-4}	13	2.0, taper	0.41″ × 0.37″ (86°)	2.7	0.59	59±6(††)
c–C_3H_2	$J = 6_{(1,6)}$–$5_{(0,5)}$	217.822148	39	5.934×10^{-4}	39	2.0, taper	0.41″ × 0.37″ (86°)	2.7	0.59	59±6(††)

Notes. All of the molecular data are from the Cologne Database for Molecular Spectroscopy (CDMS, Müller et al. 2005). Since we are comparing molecular lines from a variety of different sets of observations we take the errors on the integrated fluxes to be the 10% absolute flux calibration uncertainty of ALMA. For reference, the $C^{18}O$ J = 2 – 1 disk integrated flux from Fedele et al. (2017) is 3.9±0.5 Jy km s^{-1}. (*)Blended CH_3OH emission from up to six lines where the E_{up}, E_{Aul}, and g_u listed are of the strongest line $J = 6_{(-3,4)}$–$5_{(-3,3)}$. Other lines are $J = 6_{(3,3)}$–$5_{(3,2)}$, $J = 6_{(3,4)}$–$5_{(3,3)}$, $J = 6_{(4,2)}$–$5_{(4,1)}$, $J = 6_{(2,5)}$–$5_{(2,4)}$, and $J = 6_{(3,3)}$–$5_{(3,2)}$. (†)The CS J = 7–6 image was generated with a Gaussian *uv*-taper of 0.25″ and then further smoothed in the image plane with the CASA `imsmooth` task using a Gaussian kernel of 0.2″. Due to the lack of short-baseline data, we consider this flux a lower limit. (††)The flux is of two blended lines.

the molecules detected using these disk-integrated fluxes following the now standard methods (e.g. Loomis et al. 2018a). This assumes the gas is in local thermodynamic equilibrium and that the line emission is optically thin. For most species we only detect one transition, and therefore we calculate all of the column densities at 30 and 60 K for the molecules we expect to be tracing cooler gas and 100 K for the SO and CH_3OH that are emitting from the warmer inner disk. Where multiple lines are detected we take an average of the calculated column density. We exclude the H_2CO $J = 3_{(2,2)}$–$3_{(2,1)}$ and CH_3OH $J = 4_{(2,2)}$–$_{(1,2)}$ lines from this analysis as they are low S/N detections in the spectra (see Fig. C.1). Additionally, the H_2CO $J = 3_{(2,2)}$–$3_{(2,1)}$ line does not have the same emission morphology as the other two strongly detected H_2CO lines (see Fig. D.1).

We also compute radial column densities from the emission profiles presented in Fig. 2. This is done for SO, CS (using the optically thinner $C^{34}S$ and assuming $^{32}S/^{34}S$ = 22, e.g.; Wilson 1999), H_2CO, and CH_3OH as we want to investigate any radial variations in the N(CS)/N(SO) and N(CH_3OH)/N(H_2CO) ratios. Since we do not have any excitation information, we assume a fixed temperature of 60 K. The SO and CH_3OH are likely warmer than this and the CS and H_2CO may be cooler, but given the data in hand this intermediate temperature is the simplest assumption to make. Figure 3 shows the radial column densities at the native angular resolution for each of the four molecules alongside a version where the SO and CH_3OH images are convolved to the same angular resolution of the ^{34}CS and H_2CO data using CASA tool *imsmooth*. We find that the N(CS)/N(SO) ratio increases as a function of radius and the N(CH_3OH)/N(H_2CO) ratio decreases as a function of radius (see Fig. 3). These ratios in the context of the disk chemistry and forming planets in the HD 169142 disk are discussed in Sect. 4.

Table 2. Disk-averaged column densities assuming a circular emitting area of 2″ for all species aside from CH_3OH and SO where we use 0.3″.

Species	N (cm^{-2})		
	T_{ex} : 30 K	60 K	100 K
[CI]	$(5.1 \pm 0.5) \times 10^{16}$	$(5.0 \pm 0.5) \times 10^{16}$	–
DCO^+	$(3.0 \pm 0.3) \times 10^{11}$	$(3.7 \pm 0.4) \times 10^{11}$	–
DCN	$(2.6 \pm 0.3) \times 10^{11}$	$(3.1 \pm 0.3) \times 10^{11}$	–
N_2H^+	$(4.5 \pm 0.5) \times 10^{10}$	$(5.7 \pm 0.6) \times 10^{10}$	–
CS	$(3.8 \pm 0.4) \times 10^{13}$	$(8.2 \pm 0.8) \times 10^{12}$	–
$C^{34}S$	$(8.5 \pm 0.9) \times 10^{11}$	$(8.9 \pm 0.9) \times 10^{11}$	–
^{13}CS	$(2.5 \pm 0.3) \times 10^{11}$	$(2.3 \pm 0.3) \times 10^{11}$	–
SO	–	–	$(2.1 \pm 0.3) \times 10^{13(*)}$
H_2CS	$(4.2 \pm 0.4) \times 10^{12}$	$(3.5 \pm 0.4) \times 10^{12}$	–
H_2CO	$(1.0 \pm 0.1) \times 10^{13}$	$(1.6 \pm 0.2) \times 10^{13}$	–
CH_3OH	–	–	$(3.3 \pm 0.3) \times 10^{14}$
HC_3N	$(1.0 \pm 0.1) \times 10^{13}$	$(2.2 \pm 0.2) \times 10^{12}$	–
c–C_3H_2	$(5.6 \pm 0.6) \times 10^{11}$	$(8.4 \pm 0.8) \times 10^{11}$	–

Notes. A range of T_{ex} is explored for all species and from DCN, DCO^+, H_2CO, and CH_3OH. Errors in column densities are propagated from the assumed 10% uncertainty in the disk-integrated fluxes. (*)From Law et al. (2023).

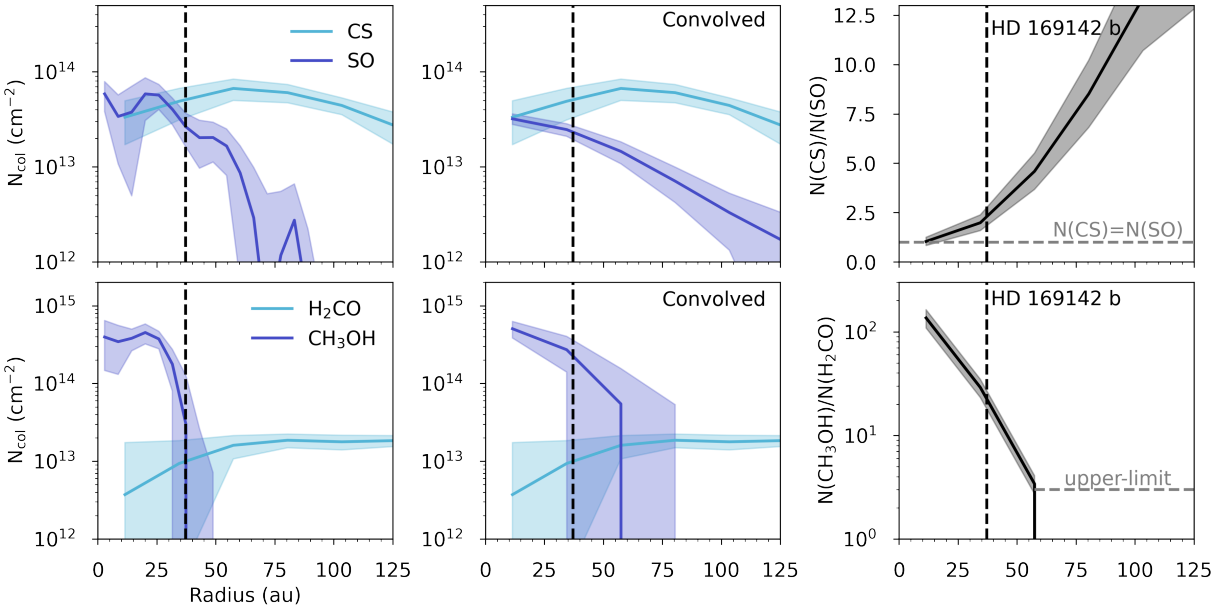

Fig. 3. Radial profiles of column densities and column density ratios for SO, CS, CH_3OH, and H_2CO in the HD 169142 disk. These are computed from the radial emission profiles in Fig. 2 assuming a temperature of 60 K. Left: At the native resolution of the data; middle: Convolved to the same beam; and right: Ratios of the convolved profiles. We show N(CS)/N(SO)=1 with a horizontal line; for H_2CO and CH_3OH we show the upper limit on the column density ratio where CH_3OH is not detected. The vertical dashed line gives the radial location of the giant planet HD 169142 b.

4. Discussion

We detected a range of molecules from the HD 169142 disk that can be used to unravel the physical and chemical conditions in the system. In this section, we discuss the locations of the CO and H_2O snowlines, the evidence for radial variations in C/O, and how this connects to the composition of the forming planet(s) in this disk.

4.1. Locating the CO and H_2O snowlines

The CO snowline in the HD 169142 disk has been investigated using observations of DCO^+ (Macías et al. 2017; Carney et al. 2018). The dust temperature in the fiducial model of this disk from Carney et al. (2018) only reaches the freeze-out temperature of CO (≈20 K) in the midplane of the very outer disk at ≈150 au and there is no complete freeze-out of CO indicating a CO snowline. In this work we present the detection of N_2H^+, which is a more robust tracer of the CO snowline (e.g. Qi et al. 2015). The N_2H^+ emission extends to ≈200 au. N_2H^+ does not solely trace the CO snowline in disks, and it can be present in the warm molecular layer of the disk where CO is photo-dissociated and N_2 is not yet photo-dissociated (van 't Hoff et al. 2017). Compared to the models presented in Anderson et al. (2019) and Trapman et al. (2022), the low N_2H^+ line flux observed towards HD 169142 relative to $C^{18}O$ is consistent with minimal CO depletion (i.e. a gas-phase CO/H_2 abundance of $\approx 10^{-4}$). Therefore, the weak N_2H^+ emission detected may be tracing the gas-phase chemistry in the upper layers of the disk atmosphere inside the CO snowline. Figure 4 compares the $C^{18}O$ J = 2−1, N_2H^+ J = 3−2, DCO^+ J = 3−2, DCN J = 3−2 and H_2CO $J = 3_{(0,3)}-2_{(0,2)}$ line fluxes observed towards the HD 169142, TW Hya, MWC 480, and HD 163296 disks. Scaled to a distance of 100 pc the N_2H^+ emission from HD 169142 is ≈10× weaker than in both of the Herbig disks and the T Tauri disk TW Hya. Relative to the $C^{18}O$ J = 2−1 line flux, the N_2H^+ is ≈5× weaker than in HD 163296 and MWC 480. The depletion of CO beyond the midplane CO snowline has been measured in the HD 163296 and MWC 480 disks, where Zhang et al. (2021) find a drop in CO abundance of at least a factor of 10 at a radius of 65 au and 100 au for each disk, respectively. In comparison, a similar drop in CO abundance is not required in the HD 169142 disk to reproduce the DCO^+ data (Carney et al. 2018). That being said, if there is a CO snowline, it is expected to be beyond the millimetre-dust rings and the currently known giant planet orbits (Macías et al. 2017; Carney et al. 2018).

We can trace the H_2O snowline indirectly under the assumption that CH_3OH is thermally desorbed from the dust grains where $T_{dust} > 100$ K. The temperature of optically thick CO gas in the millimetre-dust cavity is also >100 K, which supports this hypothesis (e.g. Leemker et al. 2022). This is also consistent with the model from Carney et al. (2018), which places the H_2O midplane snowline at ≈20 au, which is at the edge of the inner dust ring (shown in Fig. E.1).

4.2. Volatile sulphur and C/O

In the HD 169142 disk, we have detections of SO, CS, $C^{34}S$, ^{13}CS, and H_2CS. Using the ratios of the different CS isotopologues we can assess whether the main isotopologue is optically thick. The inferred column density ratios of CS/$C^{34}S$ (44 ± 10 at 30 K, 10 ± 5 at 60 K) and CS/^{13}CS (150 ± 30 at 30 K, 36 ± 8 at 60 K) compared to the ISM isotope ratios ($^{32}S/^{34}S$ = 22, $^{12}C/^{13}C$=69, e.g.; Wilson 1999) indicate optically thick CS if the emitting layer of the gas is warm ≈60 K. If the gas is cooler (30 K), then the isotopes appear to be less abundant than in the ISM, but they may emit from different layers of the disk, and therefore at different temperatures. Observation of CS J = 6−5 rather than J = 10 − 9 to match the $C^{34}S$ and ^{13}CS lines, respectively, will help break this degeneracy. The CS line is ringed and the H_2CS line follows this same spatial distribution with a H_2CS/CS ratio of 0.22 ± 0.04 at 30 K and 0.18 ± 0.04 at 60 K (assuming $N(CS) = N(C^{34}S) \times 22$). This value is consistent with what was observed for disks by Le Gal et al. (2019b), who report

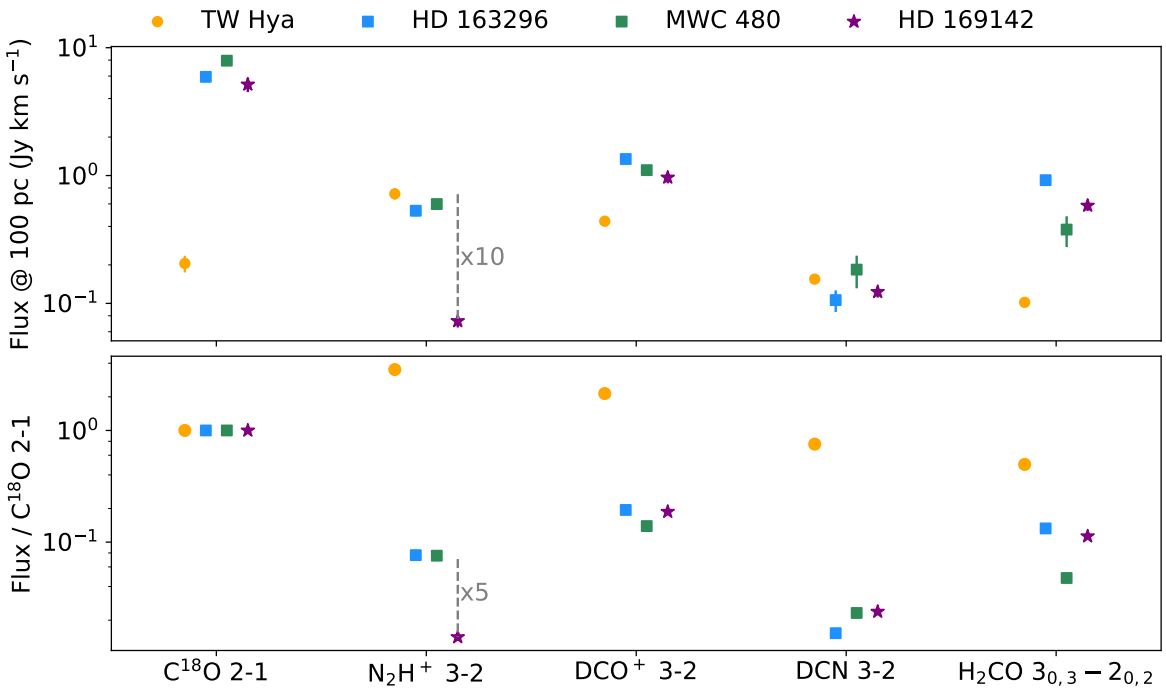

Fig. 4. Comparisons of line fluxes and line flux ratios for the TW Hya, HD 163296, MWC 480 and HD 169142 disks. Data are compiled from this work, Qi et al. (2015); Carney et al. (2018); Pegues et al. (2020); Loomis et al. (2020); Calahan et al. (2021); Öberg et al. (2021); Muñoz-Romero et al. (2023); Pegues et al. (2023). In the top panel line fluxes and their associated errors are scaled to 100 pc for each disk taking TW Hya at 60 pc, HD 169142 at 114 pc, MWC 480 at 160 pc, and HD 163296 at 101 pc (Gaia Collaboration 2018; Vioque et al. 2018).

that the H_2CS/CS ratio in disks is more similar to pre-stellar cores than protostellar envelopes and photo-dissociation regions where the H_2CS/CS values are higher. We also detect SO, which lies interior to the CS emission. This change in volatile S carrier across the disk is likely tracing the change in C/O at the H_2O snowline. Figure 3 shows that the N(CS)/N(SO) ratio is 1.0±0.2 at 10 au and then increases radially to >10 by 100 au. Since the SO data are convolved to a lower spatial resolution (0.7″), the minimum N(CS)/N(SO) is likely lower than 1.0 since the emission is more compact at 0.2″ and the CS already shows a gas cavity in the 0.7″ data. Compared to other Herbig disks, this ratio sits in the middle with Oph-IRS 48 having a disk averaged N(CS)/N(SO)<0.01 and HD 142527 a disk averaged ratio >1 (Booth et al. 2021a; Temmink et al. 2023). An elevated C/O in the outer disk gas where the CS is present is also supported by the rings of HC_3N and c−C_3H_2. Calahan et al. (2023) show with chemical models that a C/O> 1 UV-driven chemistry leads to the efficient formation of HC_3N in the gas-phase.

4.3. Organic content

We detect a number of organic molecules in the HD 169142 disk: H_2CO, CH_3OH, HC_3N, and c−C_3H_2. It is interesting to compare the distribution of H_2CO and CH_3OH as they both share a formation route on the grains (Fuchs et al. 2009). HD 169142 hosts a warm disk with $T_{\rm dust}$ > 20 K, and therefore limited CO freeze-out. This implies the inheritance of CH_3OH ices rather than in situ formation (Booth et al. 2021b). The disk temperature also favours the formation of the observed H_2CO in the gas-phase rather than on the grains (Terwisscha van Scheltinga et al. 2021). We find that the two strongest H_2CO lines we detect have central cavities with a drop in emission where the CH_3OH is detected. This difference may be a result of excitation since these lines have upper energy levels of 21 and 35 K, whereas we expect the CH_3OH to be present at temperatures >100 K. To potentially support this, the third H_2CO line we (weakly) detect has an upper energy level of 68 K and shows compact emission, such as CH_3OH (see Fig. D.1). The difference between H_2CO and CH_3OH can also be due to the gas-phase formation of the H_2CO in the outer disk, which does not occur for CH_3OH. In Fig. 3, we show the radial ratio of $N(CH_3OH)/N(H_2CO)$. Within the H_2O snowline line at 10 au this ratio is 140 ± 40, which decreases sharply to <3 beyond ≈60 au. This is similar to the trend shown for the HD 100546 disk (Booth et al. 2021b), although the peak of the ratio is lower in HD 100546. A $N(CH_3OH)/N(H_2CO)$ ratio >1 is also consistent with thermal ice desorption observed in the Class II disk Oph-IRS 48, observations of Class I protostars, and cometary ice abundances (Jørgensen et al. 2016; Bockelée-Morvan & Biver 2017; van der Marel et al. 2021). In the colder outer disk the data are not sensitive enough to detect the same non-thermally desorbed reservoir of CH_3OH as seen for HD 100546 and TW Hya where $N(CH_3OH)/N(H_2CO) \approx 1$–2 (Carney et al. 2019; Booth et al. 2021b). The H_2CO extends out to 200 au where a component of the H_2CO could originate from non-thermal desorption of H_2CO-rich ices at the edge of the millimetre-dust disk.

The H_2CO, DCO^+, and DCN line fluxes for HD 169142 are consistent with the trends derived in Pegues et al. (2023), where the Herbig disks have lower line fluxes relative to C^{18}O (a proxy for total gas mass) than the T Tauri disks, which indicates less active cold chemistry (see Fig. 4). We take the HD 169142 C^{18}O J = 2−1 line flux of 3.9 Jy km s^{-1} from Fedele et al. (2017). The similarities in the DCO^+, DCN, and H_2CO lines in the three Herbig disks may indicate that CO freeze-out does not significantly impact the primary formation and destruction routes of these species in Herbig disks.

At the edge of millimetre-dust disk is also where the rings of HC_3N and c−C_3H_2 are peaking. Ilee et al. (2021) report

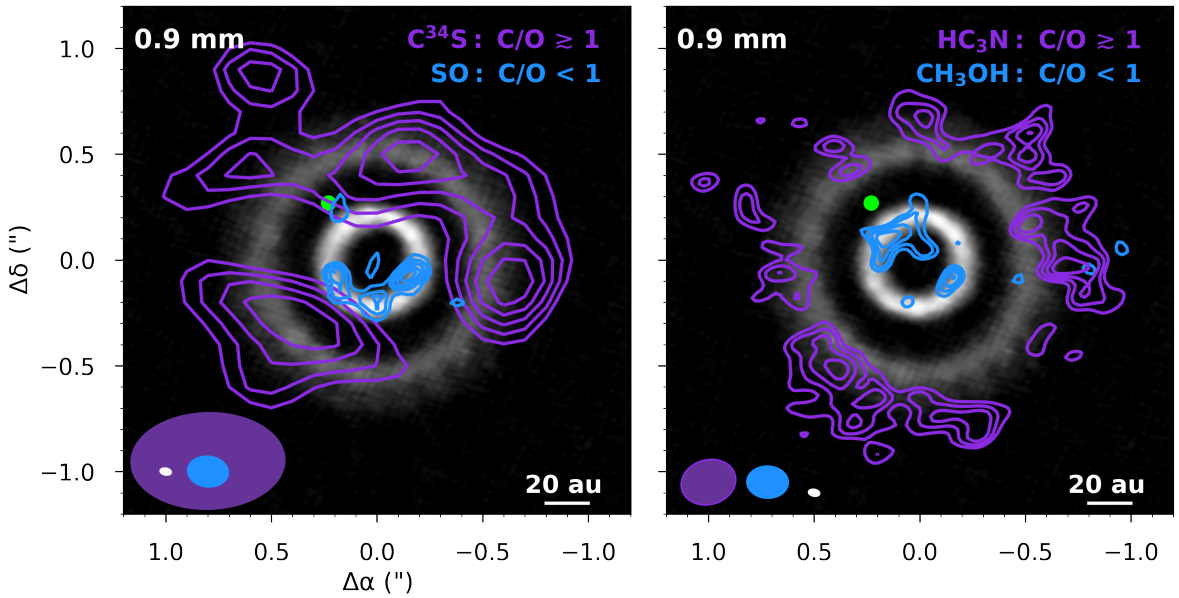

Fig. 5. HD 169142 0.9 mm continuum emission (grey-scale) with coloured contours showing the 60, 70, 80, and 90% integrated flux values for $C^{34}S$ and SO in the left panel and HC_3N and CH_3OH in the right panel. The green dot gives the location of the giant planet at 37 au (Gratton et al. 2019; Garg et al. 2022; Hammond et al. 2023). The different beams for each molecular line are shown in the same colours as the contours.

clear rings of HC_3N and c−C_3H_2 (and CH_3CN) in the AS 209, HD 163296, and MWC 480 protoplanetary disks. In comparison to HD 169142, the HC_3N and c−C_3H_2 emission rings from these sources all fall well within the radial extent of the millimetre-dust disks. However, there are some similarities between these disks. For the HD 163296 disk the peak of the H_2CO emission is just beyond the peaks of the HC_3N and c−C_3H_2 rings (Law et al. 2021; Guzmán et al. 2021; Ilee et al. 2021), and for HD 169142 we find that the H_2CO is more radially extended in than the HC_3N and c−C_3H_2. Higher angular resolution H_2CO observations are required to properly determine the relationship between the dust, H_2CO, and the large organics CH_3OH, HC_3N, and c−C_3H_2.

4.4. Connections to planet composition

Multiple complementary studies indicate that there are at least two giant planets in the HD 169142 system, one within the central millimetre-dust cavity (likely a massive companion rather than a planet) and another located in the gap between millimetre-dust rings at 37 au (HD 169142 b) (Gratton et al. 2019; Leemker et al. 2022; Garg et al. 2022; Hammond et al. 2023). Using the molecular line observations of the HD 169142 disk, we can infer the chemical make-up of the gas in the proximity of these planets. Figure 5 shows millimetre-dust emission; the expected location of HD 169142 b; and the contours tracing the emission from ^{34}CS, SO, CH_3OH, and HC_3N. Under the assumption that SO and CH_3OH trace gas with C/O<1, any planet forming within the central dust cavity will be forming within the H_2O snowline, and therefore will be able to accrete gas with a bulk C/O<1. In contrast, HD 169142 b forms beyond the water snowline and, given the temperature structure of the disk (see Fig. E.1), beyond the CO_2 snowline as well. Since the CO snowline lies well beyond the dust disk, HD 169142 b should be located within the CO snowline. From this, the most simple interpretation is that HD 169142 b is accreting gas with an elemental C/O ratio of 1.0 (Öberg et al. 2011). Figure 3 shows that the N(CS)/N(SO) ratio at the location of HD 169142 b is 2.0 ± 0.4. Compared to astrochemical models, this is broadly consistent with our interpretation of an overall C/O≈1 in this region of the disk (Semenov et al. 2018; Fedele & Favre 2020). The [CI] also traces the gas in the outer disk, and has been detected in two other Herbig disks, HD 163296 and HD 142527 (Alarcón et al. 2022; Temmink et al. 2023). Chemical models show that [CI] is expected to trace the upper layers of the disk, and can be used to determine the carbon abundance in the disk atmosphere (Kama et al. 2016). Further work to specifically model [CI] in disks will allow both comparisons of disk C/H and C/O to giant exoplanet atmospheres. The gas composition in the vicinity of the planet may be altered if the planet is locally heating the disk leading to a C/O< 1 in the gas, as suggested for HD 100546 (Booth et al. 2023) and tentatively traced by the SO line in HD 169142 (see Fig. 5; Law et al. 2023).

5. Conclusion

We have analysed the ALMA data of the HD 169142 disk and presented observations of 13 different species. Our main conclusions are as follows:

- We present the first detections of N_2H^+, CH_3OH, [CI], DCN, CS, $C^{34}S$, ^{13}CS, H_2CS, H_2CO, HC_3N, and c−C_3H_2 in the HD 169142 disk.
- The line ratios and abundance ratios of DCO^+, DCN, H_2CO, CS, and H_2CS detected in HD 169142 are consistent with observations of the other Herbig disks HD 163296 and MWC 480.
- The N_2H^+ line flux from the HD 169142 disk is low relative to HD 163296 and MWC 480. This comparison and the temperature structure in the disk model from Carney et al. (2018) indicates the lack of CO freeze-out in the HD 169142 disk, but if there is a CO freeze-out in this disk it is likely beyond the millimetre-dust disk edge (≈100 au) and out at ≈150 au.
- The detection of CH_3OH and SO from the inner disk can be explained by the sublimation of ices putting the H_2O snowline at the edge of the inner millimetre-dust ≈20 au. This is consistent with the brightness temperature of CO exceeding 100 K in this region of the disk (Leemker et al. 2022).

- HD 169142 is now the third warm Herbig disk where the signature of CH_3OH ice sublimation has been detected. Since CH_3OH needs to form in the cold phase, this further supports the hypothesis that complex ices can survive the disk formation process.
- The variation in the radial column density ratio of CS to SO supports gas-phase C/O variations in the HD 169142 disk across the H_2O snowline. The large organic molecules HC_3N and c−C_3H_2 may be tracing gas with a C/O≈1 and appear in rings at the edge of the millimetre-dust disk.
- We estimate that the giant planet HD 169142 b is forming between the CO and H_2O snowlines, and given the temperature structure of the disks likely between the CO_2 and CO snowlines. This is a region of the disk where C/O≈1.0. However, this ratio may be lowered if the planet is heating the disk locally resulting in the sublimation of O-rich ices. Future higher angular resolution observations will be able to further characterise the gas composition in the vicinity of this planet. If there is another giant planet in the central cavity <20 au this is within the H_2O snowline and therefore the planet will be accreting gas with C/O<1.

Many of the line detections presented in this work are serendipitous detections in continuum spectral windows in archival ALMA data. As continuum observations with ALMA reach higher sensitivities, the likelihood of picking up such lines increases. We urge the community to be mindful of the frequency ranges and spectral resolution (FDM mode) used for continuum observations so that if lines are detected there is the best opportunity possible to use them for science.

Acknowledgements. We thank Karin Öberg and Ewine van Dishoeck for their useful comments on this paper. This work makes use of the following ALMA data: 2012.1.00799.S, 2015.1.00806.S, 2016.1.00344.S, 2016.1.00346.S, 2018.1.01237. ALMA is a partnership of ESO (representing its member states), NSF (USA) and NINS (Japan), together with NRC (Canada), MOST and ASIAA (Taiwan), and KASI (Republic of Korea), in cooperation with the Republic of Chile. The Joint ALMA Observatory is operated by ESO, AUI/NRAO and NAOJ. We acknowledge assistance from Allegro, the European ALMA Regional Centre node in the Netherlands. Astrochemistry in Leiden is supported by funding from the European Research Council (ERC) under the European Union's Horizon 2020 research and innovation programme (grant agreement no. 101019751 MOLDISK). This work has used the following additional software packages that have not been referred to in the main text: Astropy, IPython, Jupyter, Matplotlib and NumPy (Astropy Collaboration 2022; Pérez & Granger 2007; Kluyver et al. 2016; Hunter 2007; Harris et al. 2020).

References

Alarcón, F., Bergin, E. A., & Teague, R. 2022, ApJ, 941, L24
Anderson, D. E., Blake, G. A., Bergin, E. A., et al. 2019, ApJ, 881, 127
Astropy Collaboration (Price-Whelan, A. M., et al.) 2022, ApJ, 935, 167
Banzatti, A., Pascucci, I., Bosman, A. D., et al. 2020, ApJ, 903, 124
Bean, J. L., Xue, Q., August, P. C., et al. 2023, Nature, 618, 43
Bockelée-Morvan, D., & Biver, N. 2017, Philos. Trans. Roy. Soc. Lond. Ser. A, 375, 20160252
Booth, R. A., & Ilee, J. D. 2019, MNRAS, 487, 3998
Booth, A. S., van der Marel, N., Leemker, M., van Dishoeck, E. F., & Ohashi, S. 2021a, A&A, 651, A6
Booth, A. S., Walsh, C., Terwisscha van Scheltinga, J., et al. 2021b, Nat. Astron., 5, 684
Booth, A. S., Ilee, J. D., Walsh, C., et al. 2023, A&A, 669, A53
Bosman, A. D., & Bergin, E. A. 2021, ApJ, 918, L10
Bosman, A. D., Alarcón, F., Bergin, E. A., et al. 2021, ApJS, 257, 7
Calahan, J. K., Bergin, E., Zhang, K., et al. 2021, ApJ, 908, 8
Calahan, J. K., Bergin, E. A., Bosman, A. D., et al. 2023, Nat. Astron., 7, 49
Carmona, A. 2018, in Take a Closer Look, 64
Carney, M. T., Fedele, D., Hogerheijde, M. R., et al. 2018, A&A, 614, A106
Carney, M. T., Hogerheijde, M. R., Guzmán, V. V., et al. 2019, A&A, 623, A124
Dawson, R. I., & Johnson, J. A. 2018, ARA&A, 56, 175
Du, F., Bergin, E. A., & Hogerheijde, M. R. 2015, ApJ, 807, L32
Eistrup, C. 2023, ACS Earth Space Chem., 7, 260
Fedele, D., & Favre, C. 2020, A&A, 638, A110
Fedele, D., Carney, M., Hogerheijde, M. R., et al. 2017, A&A, 600, A72
Fuchs, G. W., Cuppen, H. M., Ioppolo, S., et al. 2009, A&A, 505, 629
Gaia Collaboration (Brown, A. G. A., et al.) 2018, A&A, 616, A1
Garg, H., Pinte, C., Hammond, I., et al. 2022, MNRAS, 517, 5942
Gratton, R., Ligi, R., Sissa, E., et al. 2019, A&A, 623, A140
GRAVITY Collaboration (Nowak, M., et al.) 2020, A&A, 633, A110
Guzmán, V. V., Bergner, J. B., Law, C. J., et al. 2021, ApJS, 257, 6
Hammond, I., Christiaens, V., Price, D. J., et al. 2023, MNRAS, 522, L51
Harris, C. R., Millman, K. J., van der Walt, S. J., et al. 2020, Nature, 585, 357
Hunter, J. D. 2007, Comput. Sci. Eng., 9, 90
Ilee, J. D., Walsh, C., Booth, A. S., et al. 2021, ApJS, 257, 9
Jørgensen, J. K., Visser, R., Sakai, N., et al. 2013, ApJ, 779, L22
Jørgensen, J. K., van der Wiel, M. H. D., Coutens, A., et al. 2016, A&A, 595, A117
Kama, M., Bruderer, S., van Dishoeck, E. F., et al. 2016, A&A, 592, A83
Kluyver, T., Ragan-Kelley, B., Pérez, F., et al. 2016, in Positioning and Power in Academic Publishing: Players, Agents and Agendas, eds. F. Loizides, & B. Schmidt (IOS Press), 87
Krijt, S., Schwarz, K. R., Bergin, E. A., & Ciesla, F. J. 2018, ApJ, 864, 78
Law, C. J., Loomis, R. A., Teague, R., et al. 2021, ApJS, 257, 3
Law, C. J., Booth, A. S., & Öberg, K. I. 2023, ApJ, 952, L19
Le Gal, R., Brady, M. T., Öberg, K. I., Roueff, E., & Le Petit, F. 2019a, ApJ, 886, 86
Le Gal, R., Öberg, K. I., Loomis, R. A., Pegues, J., & Bergner, J. B. 2019b, ApJ, 876, 72
Le Gal, R., Öberg, K. I., Teague, R., et al. 2021, ApJS, 257, 12
Leemker, M., van't Hoff, M. L. R., Trapman, L., et al. 2021, A&A, 646, A3
Leemker, M., Booth, A. S., van Dishoeck, E. F., et al. 2022, A&A, 663, A23
Leemker, M., Booth, A. S., van Dishoeck, E. F., et al. 2023, A&A, 673, A7
Loomis, R. A., Cleeves, L. I., Öberg, K. I., et al. 2018a, ApJ, 859, 131
Loomis, R. A., Öberg, K. I., Andrews, S. M., et al. 2018b, AJ, 155, 182
Loomis, R. A., Öberg, K. I., Andrews, S. M., et al. 2020, ApJ, 893, 101
Macías, E., Anglada, G., Osorio, M., et al. 2017, ApJ, 838, 97
Macías, E., Espaillat, C. C., Osorio, M., et al. 2019, ApJ, 881, 159
McMullin, J. P., Waters, B., Schiebel, D., Young, W., & Golap, K. 2007, in Astronomical Data Analysis Software and Systems XVI, eds. R. A. Shaw, F. Hill, & D. J. Bell, Astronomical Society of the Pacific Conference Series, 376, 127
Miotello, A., Facchini, S., van Dishoeck, E. F., et al. 2019, A&A, 631, A69
Müller, H. S. P., Schlöder, F., Stutzki, J., & Winnewisser, G. 2005, J. Mol. Struct., 742, 215
Muñoz-Romero, C. E., Öberg, K. I., Law, C. J., et al. 2023, ApJ, 943, 35
Notsu, S., Akiyama, E., Booth, A., et al. 2019, ApJ, 875, 96
Öberg, K. I., & Bergin, E. A. 2021, Phys. Rep., 893, 1
Öberg, K. I., Murray-Clay, R., & Bergin, E. A. 2011, ApJ, 743, L16
Öberg, K. I., Guzmán, V. V., Walsh, C., et al. 2021, ApJS, 257, 1
Pegues, J., Öberg, K. I., Bergner, J. B., et al. 2020, ApJ, 890, 142
Pegues, J., Öberg, K. I., Qi, C., et al. 2023, ApJ, 948, 57
Pérez, F., & Granger, B. E. 2007, Comput. Sci. Eng., 9, 21
Pérez, S., Casassus, S., Baruteau, C., et al. 2019, AJ, 158, 15
Poblete, P. P., Cuello, N., Pérez, S., et al. 2022, MNRAS, 510, 205
Pohl, A., Benisty, M., Pinilla, P., et al. 2017, ApJ, 850, 52
Qi, C., Öberg, K. I., Wilner, D. J., et al. 2013, Science, 341, 630
Qi, C., Öberg, K. I., Andrews, S. M., et al. 2015, ApJ, 813, 128
Raman, A., Lisanti, M., Wilner, D. J., Qi, C., & Hogerheijde, M. 2006, AJ, 131, 2290
Reggiani, H., Schlaufman, K. C., Healy, B. F., Lothringer, J. D., & Sing, D. K. 2022, AJ, 163, 159
Semenov, D., Favre, C., Fedele, D., et al. 2018, A&A, 617, A28
Teague, R. 2019, J. Open Source Softw., 4, 1632
Teague, R. 2020, https://doi.org/10.5281/zenodo.4321137
Temmink, M., Booth, A. S., van der Marel, N., & van Dishoeck, E. F. 2023, A&A, 675, A131
Terwisscha van Scheltinga, J., Hogerheijde, M. R., Cleeves, L. I., et al. 2021, ApJ, 906, 111
Trapman, L., Zhang, K., van't Hoff, M. L. R., Hogerheijde, M. R., & Bergin, E. A. 2022, ApJ, 926, L2
van der Marel, N., Booth, A. S., Leemker, M., van Dishoeck, E. F., & Ohashi, S. 2021, A&A, 651, A5
van 't Hoff, M. L. R., Walsh, C., Kama, M., Facchini, S., & van Dishoeck, E. F. 2017, A&A, 599, A101
Vioque, M., Oudmaijer, R. D., Baines, D., Mendigutía, I., & Pérez-Martínez, R. 2018, A&A, 620, A128
Wang, J., Wang, J. J., Ma, B., et al. 2020, AJ, 160, 150
Wilson, T. L. 1999, Rep. Progr. Phys., 62, 143
Zhang, K., Bergin, E. A., Schwarz, K., Krijt, S., & Ciesla, F. 2019, ApJ, 883, 98
Zhang, K., Booth, A. S., Law, C. J., et al. 2021, ApJS, 257, 5

Appendix A: ALMA observations

Table A.1. Summary of ALMA observations used in this work.

Project ID	PI	Band	Date	No. Ant.	Baselines [m]	Integration Time [min]	M.R.S. ["]
2012.1.00799.S	Honda, M.	7	2015-07-26	41	15–1574	41.4	1.3
		7	2015-07-27	41	15–1574	21.2	1.4
		7	2015-08-08	43	35–1574	41.4	1.3
2015.1.00806.S	Pineda, J.	7	2015-12-06	32	19–7716	25.3	0.4
2016.1.00344.S	Pérez, S.	6	2016-10-04	40	19-3144	33.3	8.5
			2017-07-05	44	21-2647	33.2	7.7
2016.1.00346.S	Tsukagoshi, T.	8	2017-04-05	40	15-279	2.92	5.9
2018.1.01237.S	Macías, E.	7	2019-04-10	43	15-500	81.0	5.7

Appendix B: Comparisons of matched filter and *GoFish* detections of N_2H^+

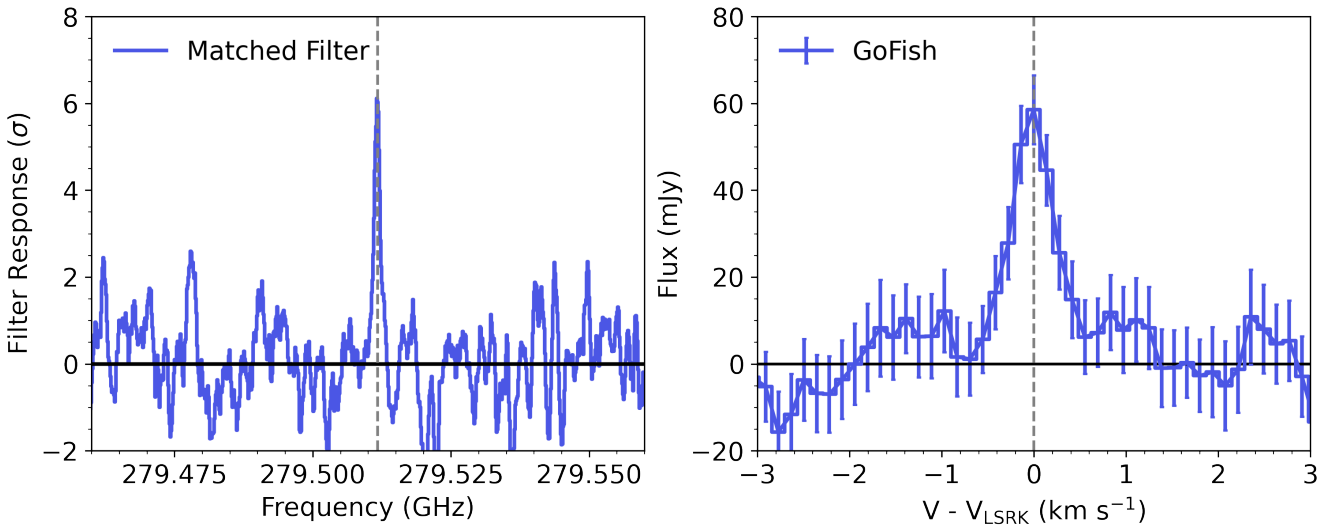

Fig. B.1. Matched filter response (left) and *GoFish* spectra (right) for N_2H^+ in the HD 169142 disk (Loomis et al. 2018b; Teague 2019). The matched filter response is for a 0–200 au Keplerian mask.

Appendix C: Spectra extracted from continuum spectral windows

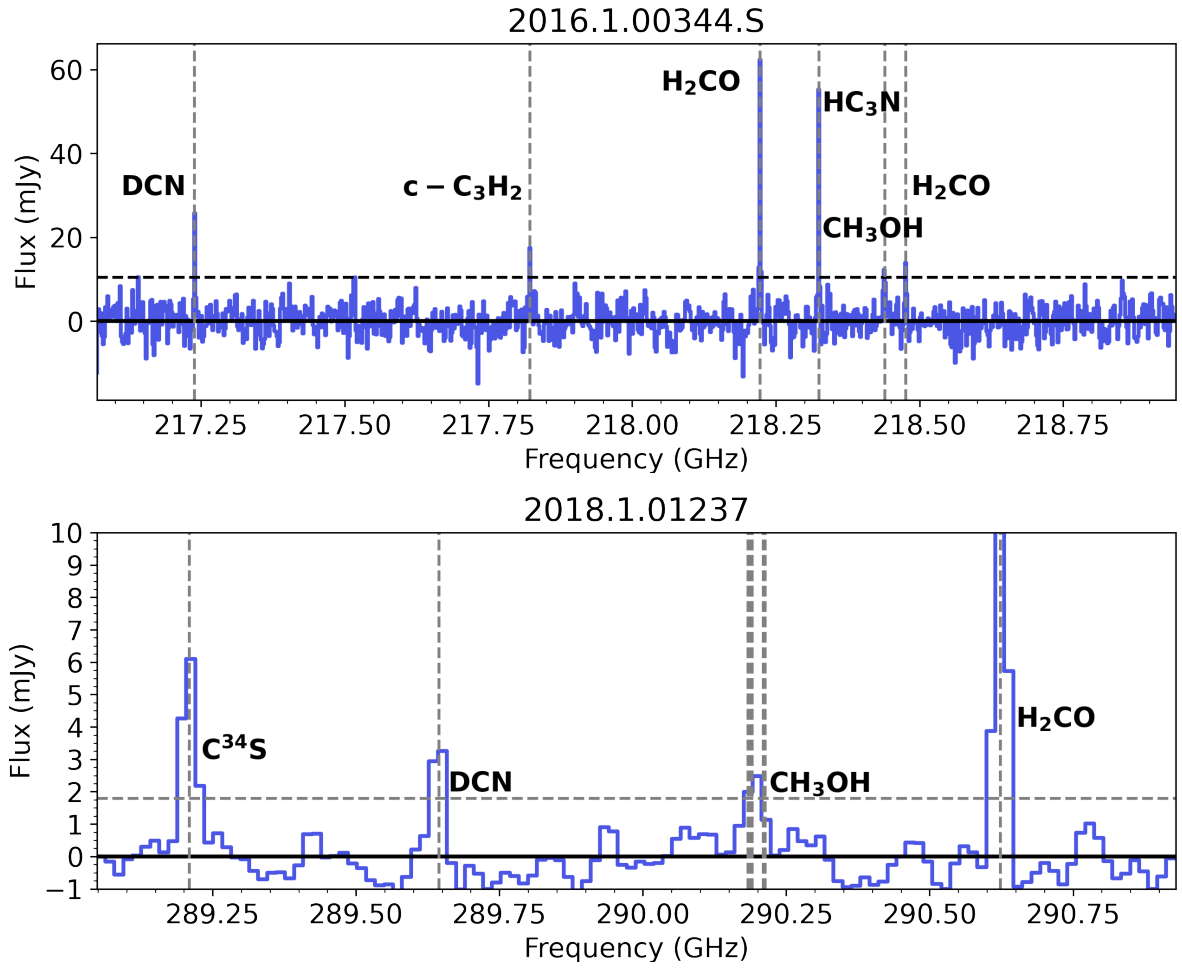

Fig. C.1. Spectra extracted from the continuum spectral windows using a 1.″0 circular aperture for the two datasets noted in the plot titles. The molecules detected are highlighted with vertical lines at their respective frequencies as listed in Table 1. The dashed horizontal line indicates the 3 σ level, where σ is calculated as the rms in the line free channels of the spectrum. To encompass the total flux of most of the lines a 2.″0 aperture is required, but the 1.″0 aperture shows both the detection of compact CH_3OH and the more extended molecules (e.g. H_2CO).

Appendix D: Supplementary line images

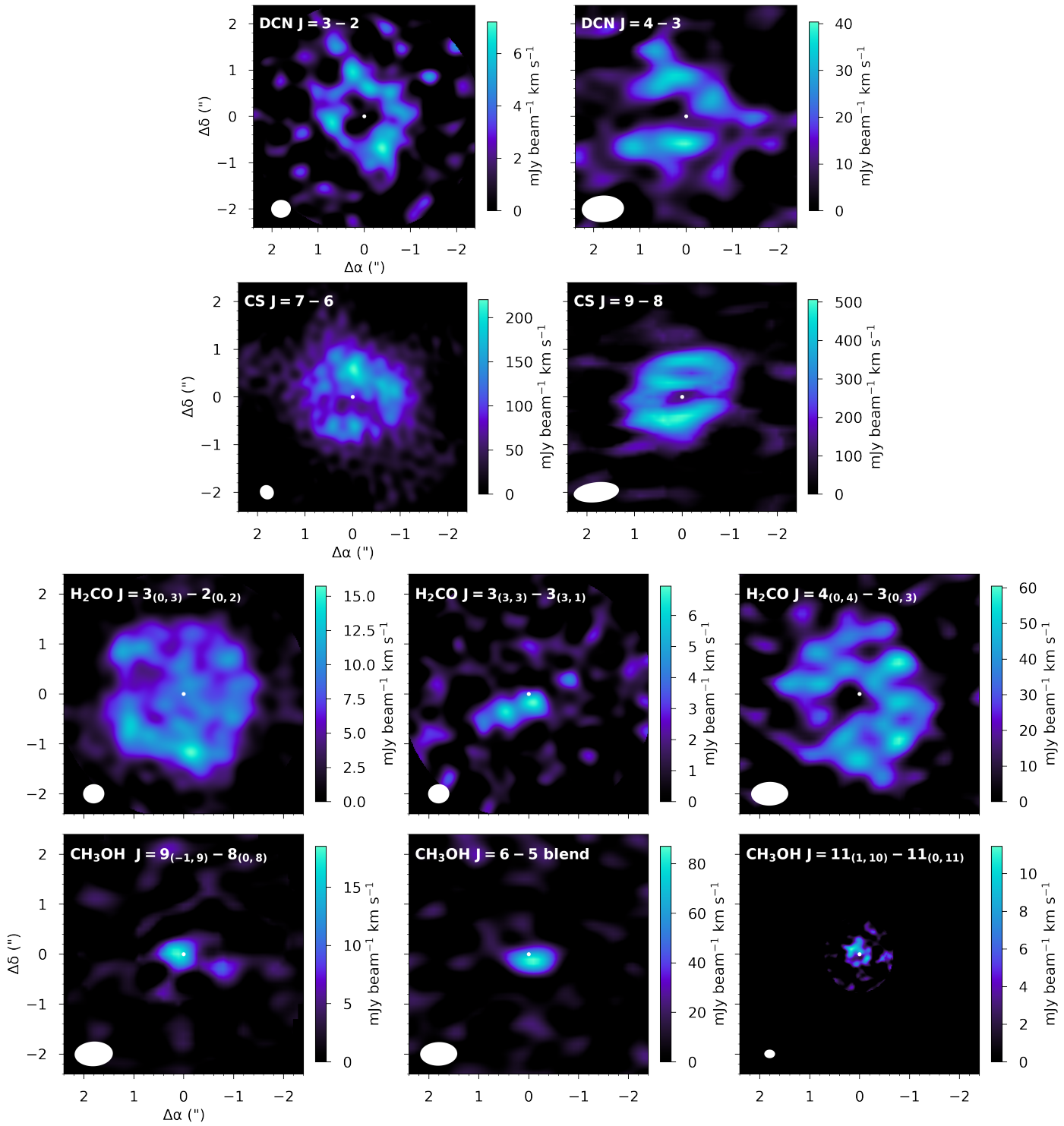

Fig. D.1. Integrated intensity maps of additional molecular transitions detected in the HD 169142 disk.

Appendix E: HD 169142 model dust temperature

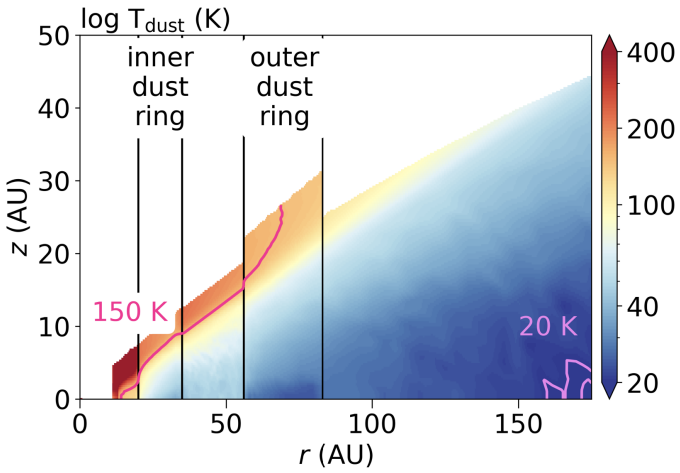

Fig. E.1. Dust temperature in the fiducial DALI model from Carney et al. (2018).